NAG5-2615
IN-48
434920

To appear in *Journal of Geophysical Research*, September 14, 1998

A preliminary model study of the large-scale seasonal cycle in bottom pressure over the global ocean

Rui M. Ponte
Atmospheric and Environmental Research, Inc., Cambridge, Massachusetts

Abstract

Output from the primitive equation model of Semtner and Chervin is used to examine the seasonal cycle in bottom pressure (p_b) over the global ocean. Effects of the volume-conserving formulation of the model on the calculation of p_b are considered. The estimated seasonal, large-scale p_b signals have amplitudes ranging from less than 1 cm over most of the deep ocean to several centimeters over shallow, boundary regions. Variability generally increases toward the western sides of the basins, and is also larger in some Southern Ocean regions. An oscillation between subtropical and higher latitudes in the North Pacific is clear. Comparison with barotropic simulations indicates that, on basin scales, seasonal p_b variability is related to barotropic dynamics and the seasonal cycle in Ekman pumping, and results from a small, net residual in mass divergence from the balance between Ekman and Sverdrup flows.

1. Introduction

Sea level pressure has played a historical and essential role in atmospheric science, from the study of storm systems and numerical weather prediction to the characterization of climate events such as the El Niño/Southern Oscillation and the North Atlantic Oscillation. Much of this prominence has been fostered by the wide coverage and availability of barometric pressure observations. Drawing a parallel with the equivalent variable for the oceans, bottom pressure (p_b), reveals a drastically different situation. There have been some focused programs that included pressure measurements at the deep sea floor, like MODE [*Brown et al.*, 1975] and more recently BEMPEX [*Luther et al.*, 1990], and a few deep observations in the Southern Ocean, mainly connected with studies of the Antarctic Circumpolar Current [e.g., *Hughes and Smithson*, 1996; *Woodworth et al.*, 1996]. Most other available observations are from relatively shallow depths. Overall, though, the data coverage is insufficient to get even a crude estimate of the seasonal cycle over the large scale.

In their work on the seasonal variability of the ocean, *Gill and Niiler* [1973; hereafter referred to as GN] assumed an ocean governed by geostrophic and Sverdrup dynamics in the interior, and Ekman dynamics near the surface, to derive a relatively simple equation for p_b of the form

$$\frac{\partial(H\csc\phi, p_b)}{\partial(\phi,\lambda)} = \csc\phi\cot\phi\frac{\partial P}{\partial\lambda} - 2\Omega a^2\rho_o\cos\phi w_E, \tag{1}$$

where H is the ocean depth, ϕ and λ are latitude and longitude, a and Ω are the Earth's radius and rotation rate, ρ_o is a mean ocean density, w_E is the Ekman pumping velocity, and P is the potential energy of the water column per unit area, defined as

$$P = \int_{-H}^{0} g\rho z dz, \tag{2}$$

with g and ρ being the acceleration of gravity and ocean density, respectively. Variables in (1-2) represent deviations from a time mean. The p_b equation should be valid for seasonal and long spatial scales (~1000 km or longer), away from western boundary regions. The two terms on the right represent, respectively, baroclinic processes associated with density changes over the water column, and forcing by the wind stress curl. For given P and w_E fields, integration along f/H contours ($f = 2\Omega\sin\phi$) from the eastern boundary yields p_b; the method fails in regions of closed f/H contours. GN found that, over the tropics, the potential energy term is important and baroclinic effects play more of a role, but poleward of 30° latitude, the w_E term dominates. Thus, the barotropic response to Ekman pumping at mid and high latitudes should play a leading role in the dynamics of seasonal fluctuations in p_b. Their theory remains essentially untested to date due to lack of appropriate data.

The ability to characterize fluctuations in p_b and understand the underlying dynamics has become increasingly important in recent years. The advent of global altimetry has highlighted the complementary nature of sea level (ζ) and p_b observations made clear by GN. Knowing both ζ and p_b could lead to more accurate estimates of density (or conversely steric height) fluctuations over the water column, and e.g. the possibility for differentiating between eustatic and steric contributions to global mean sea level trends. In some cases, improved estimates of surface heat fluxes would be possible [e.g., *Wang and Koblinsky*, 1997]. It has also become clear that the interaction of p_b signals with topography leads to important transfers of momentum between the ocean and solid Earth, on both short and long spatial scales [e.g. *Holloway*, 1992; *Ponte and Rosen*, 1994]. Knowledge of p_b is of equal importance for many other current geophysical problems, be it the determination of loading effects on the solid Earth [*vanDam and Herring*, 1994] or the interpretation of satellite geodesy measurements in terms of the Earth's variable gravity field [*Dong et al.*, 1996].

Given its broad geophysical relevance, there is a clear need for better understanding the variability in p_b. The subject gains increased significance in light of the planned launching, in a few years, of the Gravity Recovery and Climate Experiment (GRACE) satellite mission, dedicated to the study of the Earth's gravity field. Knowledge of p_b field may be improved through indirect estimation using simple theories such as that of GN, or more complex modeling efforts, but such studies have been rare. In this paper, we attempt a characterization of the large-scale, seasonal cycle in p_b, as simulated by the model of *Semtner and Chervin* [1992]. Some subtle issues in diagnosing p_b from model sea level and density fields are discussed first. The seasonal cycle in p_b is then analyzed and the underlying dynamics are examined, in comparison with simulations from a simpler, barotropic model, and in relation to wind stress forcing.

2. Calculating Bottom Pressure

In most primitive equation ocean models, p_b is not carried as a prognostic variable and must instead be diagnosed from the sea level and density fields. From integration of the hydrostatic equation over the whole water column, p_b is given by

$$p_b = g\int_{-H}^{\zeta} \rho dz + p_a \cong g\rho_o\zeta + g\int_{-H}^{0} \rho dz + p_a \qquad (3)$$

where p_a is the surface atmospheric pressure. Given the general tendency for an inverted barometer (IB) sea level response to p_a [*Ponte*, 1993; *Gaspar and Ponte*, 1997], we assume without loss of generality that $\zeta = \zeta^{ib} + \zeta'$, i.e., IB term plus dynamic signals ζ' related to pressure, wind, or any other forcing, where as usual

$$\zeta^{ib} = \frac{1}{g\rho_o}(\overline{p_a} - p_a) \qquad (4)$$

and $\overline{p_a}$ is the averaged pressure over the global oceans (overbar will denote spatially averaged quantities throughout the paper). Then (3) reduces to

$$p_b = g\rho_o\zeta' + g\int_{-H}^{0} \rho dz + \overline{p_a}. \qquad (5)$$

For later use, it is convenient to normalize (5) by $g\rho_o$ to obtain

$$\frac{p_b}{g\rho_o} = \zeta' - \zeta_\rho + \overline{\zeta_a}. \qquad (6)$$

All terms have units of length, with ζ_ρ being the steric height, and $\overline{\zeta_a}$ being the signal in centimeters of water equivalent to $\overline{p_a}$. Throughout the paper, bottom pressure will refer to the normalized pressure in (6) in centimeters of water.

The diagnoses of p_b from (3) or (6) must be consistent with the model dynamics and thermodynamics, and the treatment of the boundary forcing. In this regard, two issues need to be taken into account. First, under the IB assumption, p_a forcing is neglected in most modeling efforts. Thus, for all purposes, p_a is set to zero and its effects on p_b, represented by $\overline{\zeta_a}$, are not considered, as they are not important dynamically. For applications requiring "true" p_b (as measured by a pressure gauge), estimates of $\overline{\zeta_a}$ would have to be obtained from available atmospheric data.

A second, more important issue in calculating p_b has to do with the fact that most current ocean models use a continuity equation that implies volume conservation, i.e., $\overline{\zeta'} = 0$ [*Greatbatch*, 1994]. However, in reality ocean volume (or for that matter ocean mass) is not strictly conserved. One way for volume changes to happen is through the expansion or contraction of water parcels associated with any density changes. In volume-conserving models, changes in density are not accompanied by corresponding volume changes. Thus, for example, a uniform warming of the global ocean, with no changes in mass involved, would still show up as a signal in p_b, because the changes in ζ_ρ are not compensated by changes in ζ'.

To correct for the missing physics, one needs to consider how the ocean reacts to the unmodeled volume changes. A simplified approach to the problem is discussed in detail by *Greatbatch* [1994] and *Mellor and Ezer* [1995]. Volume changes act essentially as a barotropic load on the ocean. Under the assumption of an equilibrium adjustment and decoupling between barotropic and baroclinic processes, the unmodeled volume changes translate into a spatially homogeneous sea level signal given by

$$\delta\overline{\zeta_\rho} = -\frac{1}{A}\int_V \frac{\delta\rho}{\rho_o} dV \qquad (7)$$

(A and V are the surface area and volume of the global ocean), and involving the averaged density or steric height changes over the global ocean. Here, we shall take this correction to be valid for the seasonal time scale. At these periods, the equilibrium hypothesis likely holds [see *Ponte*, 1993]. We note, however, that the assumption of barotropic and baroclinic decoupling needs more careful future investigation.

Another way for effecting oceanic volume changes is through freshwater fluxes at the atmosphere and land interfaces. These effects are, however, not represented in volume-conserving models. In fact, the freshwater flux condition is usually implemented as a restoring to observed surface salinity fields, involving a virtual salt flux instead of a real freshwater flux (see *Huang* [1993] for a detailed treatment of these issues). Again under the same assumptions used to arrive at (7), the missing effects of real freshwater fluxes on sea level can be approximated by

$$\overline{\zeta_q} = -\frac{1}{A}\int_A \int Q dt\, dA, \qquad (8)$$

which involves the time-integrated, spatial average of the freshwater flux Q (evaporation minus precipitation and runoff). Any net Q is basically spread uniformly over the global oceans, with corresponding effects on p_b.

The sea level correction factor $\delta\overline{\zeta_\rho}$, defined by (7), is easily calculated from respective model density fields. On the other hand, calculation of $\overline{\zeta_q}$ and

$\overline{\zeta_a}$ requires averaged Q and p_a data, either from climatologies or atmospheric operational products, that are likely to have large uncertainties. Their treatment will not be attempted here, but there are a couple of points worth discussing for future reference. First, one should note that $\overline{\zeta_q}$ and $\overline{\zeta_a}$ are likely related, to the extent that changes in the mean atmospheric pressure over the oceans may involve variability in the atmospheric water content, through evaporation and precipitation processes, besides mass shifts from land- to ocean-covered regions and vice versa. Therefore, $\overline{\zeta_q}$ and $\overline{\zeta_a}$ effects should be considered together and estimated in a consistent manner. In particular, $\overline{\zeta_a}$ should be calculated based on p_a values that fully represent effects of atmospheric water content, which is not likely the case with at least some of the current operational products [*van den Dool and Saha*, 1993]. Second, effects of $\overline{\zeta_q}$ and $\overline{\zeta_a}$ on p_b may not be negligible. Operationally derived p_a values point to a seasonal cycle in $\overline{\zeta_a}$ with peak-to-peak amplitudes of 0.5–1 cm [*Ponte*, 1993; *Wunsch and Stammer*, 1997]; similar seasonal amplitudes for $\overline{\zeta_q}$ are obtained from available Q climatologies. These values may seem small, but as discussed next, are of the same order of magnitude of dynamically relevant seasonal signals in p_b.

3. Model Estimates of the Seasonal Cycle in p_b

In the absence of appropriate data sets to characterize in detail the large-scale, seasonal cycle in p_b, we examine such fields as determined from output of the Parallel Ocean Climate Model (POCM) of *Semtner and Chervin* [1992]. We use monthly averaged output from the so-called POCM_4B run, which is described in detail and analyzed in comparison with observations by *Stammer et al.* [1996]. Forcing for this run consisted of 3-day averaged wind stresses calculated from European Centre for Medium-Range Weather Forecasts (ECMWF) twice-daily wind fields, ECMWF-based monthly mean heat fluxes from *Barnier et al.* [1995], and restoring conditions to *Levitus et al.* [1994] for the surface temperature and salinity fields. The POCM output thus represents signals in ζ' and ζ_ρ related to both mechanical wind stress forcing and thermodynamical forcing, but not pressure forcing. Given the model's volume-conserving formulation, all the points discussed in the previous section are relevant in interpreting the calculated p_b fields.

The model was run initially for eight years (1987–1994). Monthly averaged temperature, salinity, and sea level fields for this period were used in (6) to calculate time series of p_b at each model grid point (spacing of 0.4° in longitude and $0.4° \cos\phi$ in latitude). Given the focus on large scale patterns, averages over 4°x4° boxes were constructed and used in the analyses. In addition, to minimize any effects of transient adjustment of the model fields to the new boundary forcing over the initial period, the analysis is restricted to the last six years of output (1989–1994).

Before analyzing the spatial character of the seasonal variability, the influence of volume effects associated with $\delta\overline{\zeta_\rho}$ are examined. Figure 1 shows the time series of $\delta\overline{\zeta_\rho}$, calculated by integrating the density field over the volume of the model as in (7), with $\rho_o = 1.03$ g/cm^3 and $A = 3.47 \times 10^{18}$ cm^2, the surface area of the model ocean. There is a long term trend of -2 cm over the six year period (approximately 3 mm/year), which is fairly linear over the first four years and tends to flatten out in the last two years. Models are known to have a tendency to drift with time, due to slow diffusive adjustment, incompatibilities in boundary forcing and model physics, etc. (see *Stammer et al.* [1996] for a brief discussion of drifts in POCM), and the implicit decrease in global mean sea level in Fig. 1 (model ocean is getting denser) seems too large to be realistic. Examination of these trends should be an important consideration for studies of interannual and lower frequency variability in p_b, but need not concern us in the study of the seasonal cycle.

Superposed on the long term trend in Fig. 1, there is a clear seasonal cycle in $\delta\overline{\zeta_\rho}$ with peak-to-peak amplitudes of approximately 0.3–0.4 cm, and minimum occurring around August. This signal is a measure of hemispheric asymetries in the ocean-land distribution and the seasonal cycle in steric height. *Mellor and Ezer* [1995] have calculated $\delta\overline{\zeta_\rho}$ from available hydrographic data and estimate a seasonal cycle with a peak-to-peak amplitude of approximately 0.8–1 cm, and minimum in July (see their Fig. 11). The tendency of POCM to underestimate the seasonal cycle in steric height, apparently due to lack of proper heat uptake by the mixed layer, results in a weaker seasonal signal in $\delta\overline{\zeta_\rho}$, and the phase shift by approximately one month with respect to the observations may be partly due to phase errors of the forcing ECMWF heat fluxes [*Stammer et al.*, 1996]. The different $\delta\overline{\zeta_\rho}$ may of course be also due to the climatological, sparse hydrographic records used in Mellor and Ezer's calculation, as opposed to the 6-year, dense sampling of the model.

The p_b fields analyzed here include the model calculated $\delta\overline{\zeta_\rho}$ term shown in Fig. 1. After removing means and trends from each p_b time series, values were averaged for each season (December-February, March-May, June-August, and September-November). The corresponding mean seasonal variability in p_b over the 6-year period of model output is shown in Fig. 2. Most of the deep ocean, including tropical latitudes, exhibit p_b fluctuations on the order of 1 cm or smaller. (Note that these amplitudes are of the same order of magnitude of the seasonal cycle in $\delta\overline{\zeta_\rho}$; the effects of $\delta\overline{\zeta_\rho}$ should thus be taken into account in the study of p_b, in contrast with their less important role for the variability in ζ.) Larger variability is seen over the Southern Ocean, the western North Pacific, and near boundary regions, particularly over shallow depths (e.g., North Sea, Bering Sea, Sea of Okhotsk, South China Sea), where amplitudes of a few centimeters are attained.

The large, basin scale character of seasonal p_b signals is striking. The Atlantic, Indian, and to some extent the Southern Ocean tend to show single sign patterns. In northern winter, most of the Atlantic and Southern Oceans show a positive mass anomaly, with the Pacific and Indian Oceans having a negative anomaly. The pattern is reversed in northern summer. Besides the apparent seasonal interbasin mass exchange, there is a clear oscillation in the North Pacific, with a node at approximately 30°N, which suggests seasonal strengthening of the depth-averaged gyre circulation in northern winter and spring, and mass exchanges between subtropical and higher latitudes.

To assess the seasonal variability in Fig. 2 as a function of frequency, Fig. 3 shows the power spectrum of p_b, calculated by averaging the periodogram over all grid boxes in the model. Each time series was detrended and tapered using a cosine bell function over 10% of the points on each end, prior to Fourier transformation. Detrending does decrease the power slightly at the first two harmonics (6 and 3 years), but has no effect on higher harmonics. The p_b spectrum shows a large dominant peak at the annual period, and a weaker peak at the semiannual period. Besides these peaks, the spectrum exhibits a dependence on frequency close to $\omega^{-0.5}$. The important contribution of the annual time scale to the seasonal variability in p_b, seen in Fig. 2, is clear.

Given the focus of many studies on the annual period, we show in Plate 1 the amplitude and phase of the annual cycle in p_b, calculated by simply Fourier transforming each time series after detrending. Most of the features discussed in relation to Fig. 2 are present in Plate 1. The annual cycle has amplitudes smaller than 1 cm over most of the global oceans, with higher values (1–3 cm) over the Southern Ocean and the western North Pacific, and over most of the shallow coastal regions in the model. The phase exhibits, for the most part, a large scale pattern: the lack of a distinct phase opposition between the Northern and Southern Hemispheres, observed in the case of ζ' and ζ_ρ, is most striking. Maximum p_b values in the Atlantic and Pacific Oceans occur mostly in the northern winter (Dec–Feb) and summer (Jun–Aug) seasons, respectively. Thus, the Atlantic and the Pacific appear to fluctuate approximately out of phase, as noted by *Stammer et al.* [1996], based on the averaged p_b field over the Atlantic and Pacific Oceans (see their Fig. 15).

Before attempting to interpret the seasonal p_b signals, it is also useful to examine the relation between p_b and ζ' by calculating

$$\mathcal{A} = \frac{(g\rho_o)^{-1}\mathcal{F}(p_b)}{\mathcal{F}(\zeta')}, \qquad (9)$$

which is essentially the admittance between p_b and ζ', with $\mathcal{F}$ denoting Fourier transform. In physical terms, $\mathcal{A}$ quantifies how much of a bottom pressure signal results from a sea level load at the surface. From (6), one expects $|\mathcal{A}| < 1$ if ζ_ρ and ζ' are correlated. Likewise, phases near zero indicate a simple in-phase relationship among p_b, ζ', and ζ_ρ. The amplitude and phase of $\mathcal{A}$ for the annual period are shown in Plate 2. Variability in p_b is weak relative to ζ', with $|\mathcal{A}| < 0.4$ over most of the oceans, away from shallow regions and the Southern Ocean. The small p_b amplitudes are expected as a result of the well-known correlation between ζ' and ζ_ρ. There is, however, extensive regions, particularly in the Southern Ocean where $|\mathcal{A}| > 0.4$. Over most shallow coastal regions, strong correspondence between p_b and ζ' is indicated by amplitudes near unity and phases near zero. These results most likely indicate the essentially barotropic nature of variability in these regions. A tendency for nearly in-phase behavior is clear in the Southern Ocean and the North Pacific (north of $\sim 30°$), but phases span the whole range. In particular, the approximately out-of-phase behavior over equatorial Pacific regions is worth noting, as indicative of the presence of first (or more precisely odd) baroclinic mode variability [e.g., *Brown et al.*, 1975]. The regional dependence of the annual admittance in

Plate 2 suggests a complex relation between p_b and ζ' and the difficulty in extracting information about p_b from the sea level fields alone.

4. Dynamics and Forcing of Seasonal Variability in p_b

As discussed in the Introduction, the importance of barotropic dynamics and wind stress curl forcing for large-scale, seasonal variability in p_b at mid and high latitudes was pointed out by GN. Model results in Fig. 2 are qualitatively similar to the North Atlantic and North Pacific estimates of GN (see their Fig. 3), but more general evidence for the importance of barotropic dynamics to the seasonal p_b variability can be obtained by comparing the POCM results to those from a recent run of the near-global, shallow-water model of *Ponte* [1993]. For details about model formulation, resolution, friction, etc., the reader should consult *Ponte* [1993] and *Gaspar and Ponte* [1997]. The available model output is from a run originally performed for other purposes and forced by four-times daily reanalysis wind stress and pressure fields from the National Centers for Environmental Prediction (NCEP) for the years 1993–1995, with a spinup period taken to be the last two months in 1992. Thus, ζ' represents the effects of both pressure and wind stress, but the latter dominates at the seasonal time scale [*Ponte*, 1994]. For the barotropic model, there is of course no role for thermodynamics, ζ_ρ is assumed constant, and calculation of p_b is equivalent to that of ζ'.

From the four-times daily model output, seasonal means of ζ' for the months Dec-Feb, Mar-May, Jun-Aug, and Sept-Nov were calculated. The resulting seasonal variability, based on years 1993–94, is shown in Fig. 4 for comparison with POCM results derived for the same 1993–94 period and shown in Fig. 5. The comparison is qualitative, as different operational products were used for the forcing fields in the two models, in addition to differences in resolution, topography, coastal geometry, etc. Nevertheless, besides a noticeable tendency for stronger signals in the barotropic model, the similarities between the POCM and barotropic results are clear. Correspondence between patterns of positive and negative p_b anomalies, and regions of larger and smaller amplitudes, is qualitatively good, especially for the winter and summer seasons. The western intensified, North Pacific oscillation between subtropical and higher latitudes is particularly well reproduced in the barotropic results.

Some of the characteristics of the p_b seasonal variability in Figs. 4 and 5 can be traced to the nature of the wind stress curl and the corresponding Ekman pumping fields in (1). Figure 6 shows the seasonal variability of the forcing w_E term in (1), calculated from monthly averages of the NCEP wind stress fields for the years 1993-94 that were used to force the barotropic model. Derivatives of the wind stress involved in the calculation were evaluated at every grid point using centered differences; the calculation was confined to latitudes poleward of 5°, as Ekman theory formally breaks down at the equator. Without attempting a full integration along f/H contours as done by GN, we note that the seasonal forcing signals are generally stronger and more zonally homogeneous in the North Pacific than in the North Atlantic. These two factors provide for the stronger p_b variability and the clear dipole pattern in the North Pacific, as compared to the North Atlantic (the longer extent of the Pacific may also lead to stronger variability toward the western boundary). More generally, there is qualitative correspondence between the positive and negative large scale patterns of the w_E and p_b fields, respectively, and vice versa, which is consistent with (1). The correspondence is particularly good for seasons and basins for which the w_E fields are more spatially homogeneous.

The relation between p_b and w_E is also apparent when examining their frequency spectra. It can be easily shown from (1) that, if the spectrum of w_E is separable in frequency and wavenumber, i.e.,

$$\phi(K,\omega) \sim \phi_1(K)\phi_2(\omega) \tag{10}$$

then the frequency dependency of the p_b spectrum is simply given by $\phi_2(\omega)$. Given that the spectrum of w_E is essentially that of the wind curl, the approximation in (10) is a reasonable one at low frequencies [e.g., *Willebrand et al.*, 1980]. We have calculated the periodogram of the w_E term in (1) at every grid point (again excluding latitudes within 5° of the equator) and averaged them together to obtain the frequency spectrum shown in Fig. 7. The frequency dependency of that spectrum is remarkably similar to the spectrum of p_b shown in Fig. 3, both in its general background shape (close to $\omega^{-0.5}$) and in the relative height of the peaks at annual and semiannual periods.

Seasonal fluctuations in p_b field, highlighted in Fig. 2 and Plate 1, represent large-scale divergence or convergence of mass brought about by the seasonally varying flow field. Horizontal oceanic motions are largely nondivergent, however, and only a small divergence is involved in effecting p_b changes. For example, to accumulate 1 cm of water over a 10^4x10^4 kilometer area in six months, one needs only a net transport of $\sim 6\times10^4$ m^{3}s^{-1}, much smaller than typical horizontal transports in the ocean. To explore the dynamics behind the divergent mass fluxes leading to the p_b signals, it is useful to consider a more general form of (1), which accounts for more terms in the divergence field. The derivation is given in Appendix A using Cartesian coordinates and neglecting nonlinear and dissipation effects for simplicity. The equation for p_b is

$$\frac{p_{b_t}}{g} + J\left(p_b, \frac{H}{f}\right) - \frac{f_y}{f^2}P_x = \left(\frac{\tau^y}{f}\right)_x - \left(\frac{\tau^x}{f}\right)_y - \rho_o Q + \mathcal{O}\left[\frac{\omega}{f}\right] \text{ terms.} \qquad (11)$$

As pointed out in Appendix A, (11) associates local mass divergence, represented by p_{b_t}, with four different processes: geostrophic flow divergence due to variable f and H, which includes the baroclinic term P_x; Ekman flow divergence forced by the wind stress; mass fluxes at the surface due to Q; and ageostrophic effects of $\mathcal{O}[\omega/f]$ relative to the geostrophic term.

Introducing a spatial scale of motion L, p_{b_t} term is $\mathcal{O}[(\omega/f)(L/L_R)^2]$ relative to geostrophic term, where $L_R = \sqrt{gH}/f$ is the external Rossby radius ($\sim$ 2000 km). Seasonal Q forcing is generally negligible compared to the Ekman terms. For seasonal time scale and away from the equator ($\omega/f \ll 1$), and for typical $L \sim$ 1000 km, one has the traditional quasi-steady Sverdrup balance, as in (1), with wind-driven Ekman divergence being for the most part balanced by geostrophic flow divergence. The net residual divergence is associated with small geostrophic flow correction to the Sverdrup solution, at scales larger than L_R. Basin-scale signals discussed in Fig. 2 are likely dominated by these processes. At scales shorter than L_R, divergence from $\mathcal{O}[\omega/f]$ ageostrophic effects should also become important, as well as dissipation and nonlinear effects not treated in (11).

5. Final remarks

It is difficult to assess the realism of the model p_b fields in Fig. 2 in the absence of global pressure records. From the available point measurements over the deep ocean, only a few are longer than one year [*Woodworth et al.*, 1996; *Mofjeld et al.*, 1996]. The observations just to the east of the Drake Passage, analyzed by *Woodworth et al.* [1996], show fluctuations over a variety of time scales; amplitudes of the seasonal cycle are not provided, but visual inspection of their Figs. 5a, 6, 7, 8a is not inconsistent with amplitudes at the centimeter level. The records of *Mofjeld et al.* [1996], taken near 46°N, 130°W in the North Pacific, show substantial contamination from instrument drift after 30-day running means are applied to them (Mofjeld, personnal communication, 1997), but all indications point to seasonal amplitudes with order of magnitude similar to the records from Woodworth et al. Not much can be said quantitatively about the agreement or disagreement between model p_b and these records, except to note that observed values seem larger than (but of the same order of magnitude of) the POCM results. Point measurements may of course relate to local processes not relevant to large-scale variability examined in the model. Direct, more quantitative evaluation of model estimates of p_b against observations must await the launching of the gravity missions currently being planned. Conversely, the seasonal fluctuations in the mass field over the oceans estimated here provide a crude measure of the oceanic signals that will need to be resolved by the planned gravity missions.

Besides comparisons with point measurements, there are other more indirect methods by which the model p_b fields can be evaluated. Given the importance of p_b variability in the excitation of Earth rotation signals, particularly seasonal polar motion [*Ponte et al.*, 1998], and also its effects on the variable gravity field, as observed by satellite tracking methods [*Dong et al.*, 1996], estimation of these oceanic effects based on the model p_b fields and comparison with other relevant geophysical observations on Earth orientation and gravity field provide an independent consistency check on the p_b fields, as shown in the case of a different ocean model by *Ponte et al.* [1998]. Analysis of the p_b fields from the POCM model in this broader geophysical context is currently being pursued by this and other investigators.

In all these comparisons, one must keep in mind that signals related to $\overline{\zeta_a}$ and $\overline{\zeta_q}$ may contribute to the local p_b measurements, and may also have a significant projection onto the integrated measurements represented by Earth rotation and large-scale gravity parameters. Given the crude estimates of $\overline{\zeta_a}$ and $\overline{\zeta_q}$ available, and depending on their relative phase, these effects may impact the estimates of the seasonal cycle in regions with p_b signals at millimeter amplitudes. Ideally, one would like to have pressure forcing and real freshwater fluxes implemented in circulation models, which would permit verification of the equilibrium response assumption at seasonal time scales and examination of higher frequency variability where that assumption becomes less useful [*Ponte* , 1993].

Finally, regarding the inferrence of surface heat fluxes or heat content in the water column from altimetry sea level records, as attempted recently by ***Wang and Koblinsky*** [1997], ***Chambers et al.*** [1997], and also ***White and Tai*** [1995], Plate 2 provides a crude estimate of the error induced by neglecting contributions to ζ which are truly related to p_b and not ζ_ρ, for the annual cycle. Depending on the region, estimates may easily be in error by 20 to 40%. However large these values may seem, the sea level-based estimates are still meaningful given the large uncertainties in the surface heat fluxes and the lack of sufficient hydrographic data sampling to estimate heat content. The possibility of improving those estimates by using model-derived p_b fields is, nevertheless, noted.

Appendix A: Derivation of General Equation for p_b

Starting from the linearized horizontal momentum and continuity equations, vertical integration over the full depth H leads to

$$
\begin{aligned}
u_t - fv &= -\frac{1}{\rho_o H}\int_{-H}^{0} p_x dz + \frac{\tau^x}{H\rho_o} \\
v_t + fu &= -\frac{1}{\rho_o H}\int_{-H}^{0} p_y dz + \frac{\tau^y}{H\rho_o} \qquad (A1) \\
\zeta_t + (Hu)_x + (Hv)_y &= \zeta_{\rho_t} - Q
\end{aligned}
$$

Here, u and v are depth-averaged flows, ζ is sea level, ζ_ρ is steric height, and Q denotes freshwater flux (evaporation minus precipitation and runoff). We work with Cartesian coordinates and neglect bottom and lateral dissipation effects for simplicity. The ocean is acted upon by surface wind stresses $\tau^{x,y}$.

To write (A1) in terms of p_b, one needs to work on the pressure integrals. Moving the derivative outside the integral, and using the fact that

$$
p(z) = p_b - g\int_{-H}^{z} \rho dz
$$

the integrals become

$$
\int_{-H}^{0} p_{x,y} dz = \left(Hp_b - g\int_{-H}^{0} dz \int_{-H}^{z} \rho dz'\right)_{x,y} - p_b H_{x,y}
$$

The double integral can be integrated by parts and after carrying out the derivatives, we have simply

$$
\int_{-H}^{0} p_{x,y} dz = Hp_{b_{x,y}} + P_{x,y} \qquad (A2)
$$

with P as defined in (2).

With the use of (A2) and the hydrostatic relation

$$
\frac{p_b}{g\rho_o} = \zeta - \zeta_\rho \qquad (A3)
$$

(effects of p_a are neglected here), we can write (A1) as

$$
\begin{aligned}
u_t - fv &= -\frac{p_{b_x}}{\rho_o} - \frac{P_x}{H\rho_o} + \frac{\tau^x}{H\rho_o} \\
v_t + fu &= -\frac{p_{b_y}}{\rho_o} - \frac{P_y}{H\rho_o} + \frac{\tau^y}{H\rho_o} \qquad (A4) \\
\frac{p_{b_t}}{g\rho_o} + (Hu)_x + (Hv)_y &= -Q
\end{aligned}
$$

These equations are very similar to the linear shallow-water equations forced by wind stress and freshwater fluxes, with p_b replacing ζ and extra forcing terms $P_{x,y}$ associated with baroclinic effects. With time dependence of the form $e^{i\omega t}$, it is straightforward to solve the momentum equations for u, v and substitute in the continuity equation to get a very general, but complicated, equation for p_b. For seasonal time scales and away from the equator, i.e., $\omega \ll f$, and without explicitly treating $\mathcal{O}[\omega/f]$ terms arising from u_t, v_t terms in (A4), one arrives at a simpler equation:

$$\frac{p_{b_t}}{g} + J\left(p_b, \frac{H}{f}\right) - \frac{f_y}{f^2} P_x =$$

$$\left(\frac{\tau^y}{f}\right)_x - \left(\frac{\tau^x}{f}\right)_y - \rho_o Q + \mathcal{O}\left[\frac{\omega}{f}\right] \text{ terms} \qquad (A5)$$

If one partitions the flow field in the usual geostrophic and Ekman components in ($A4$), it is easy to see that the wind stress terms in ($A5$) represent the divergence of the Ekman transports, whereas the Jacobian and P terms represent the divergence of geostrophic transports. Ageostrophic effects due to u_t, v_t terms in momentum equation are represented in $\mathcal{O}[\omega/f]$ terms. Any imbalance of mass fluxes due to these Ekman, geostrophic, and ageostrophic flows, and to surface mass inputs (Q term), lead to variability in p_b.

Acknowledgments. The author is grateful to A. Semtner and R. Chervin for making their model output available, and to R. Tokmakian, K. Cady-Pereira, and P. Nelson for help with data sets and model output. One anonymous reviewer helped clarify the interpretation. This work was initiated during an extended stay at the Groupe de Recherche en Géodésie Spatiale (UMR5566), in Toulouse, France, and then continued at AER under support from the NASA EOS project (grant NAGW-2615), with additional support from NASA contract NAS5-97270.

References

Barnier, B., L. Siefridt, and P. Marchesiello, Thermal forcing for a global ocean circulation model using a three-year climatology of ECMWF analyses, *J. Mar. Sys.*, *6*, 363–380, 1995.

Brown, W., W. Munk, F. Snodgrass, H. Mofjeld, and B. Zetler, MODE bottom experiment, *J. Phys. Oceanogr.*, *5*, 75–85, 1975.

Chambers, D. P., B. D. Tapley, and R. H. Stewart, Long-period ocean heat storage rates and basin-scale heat fluxes from TOPEX, *J. Geophys. Res.*, *102*, 10525–10533, 1997.

Dong, D., R. S. Gross, and J. O. Dickey, Seasonal variations of the Earth's gravitational field: An analysis of atmospheric pressure, ocean tidal, and surface water excitation, *Geophys. Res. Lett.*, *23*, 725–728, 1996.

Gaspar, P., and R. M. Ponte, Relation between sea level and barometric pressure determined from altimeter data and model simulations, *J. Geophys. Res.*, *102*, 961–971, 1997.

Gill, A. E., and P. P. Niiler, The theory of the seasonal variability in the ocean, *Deep-Sea Res.*, *20*, 141–177, 1993.

Greatbatch, R. J., A note on the representation of steric sea level in models that conserve volume rather than mass, *J. Geophys. Res.*, *99*, 12767–12771, 1994.

Holloway, G., Representing topographic stress for large-scale ocean models, *J. Phys. Oceanogr.*, *22*, 1033–1046, 1992.

Huang, R. X., Real freshwater flux as a natural boundary condition for the salinity balance and thermohaline circulation forced by evaporation and precipitation, *J. Phys. Oceanogr.*, *23*, 2428–2446, 1993.

Hughes, C. W., and M. J. Smithson, Bottom pressure correlations in the south Atlantic, *Geophys. Res. Lett.*, *23,*, 2243–2246, 1996.

Levitus, S., R. Burgett, and T. Boyer, World Ocean Atlas, Vol 3: Salinity, Vol 4: Temperature, NOAA, US Dept. of Commerce, 1994.

Luther, D. S., A. D. Chave, J. H. Filloux, and P. F. Spain, Evidence for local and nonlocal barotropic responses to atmospheric forcing during BEMPEX, *Geophys. Res. Lett.*, *17*, 949–952, 1990.

Mellor, G., and T. Ezer, Sea level variations induced by heating and cooling: an evaluation of the Boussinesq approximation in ocean models, *J. Geophys. Res.*, *100*, 20565–20577, 1995.

Mofjeld, H. O., F. I. González, and M. C. Eble, Subtidal bottom pressure observed at Axial Seamount in the notheastern continental margin of the Pacific ocean, *J. Geophys. Res.*, *101*, 16381–16390, 1996.

Ponte, R. M., Variability in a homogeneous global ocean forced by barometric pressure, *Dyn. Atmos. Oceans*, *18*, 209–234, 1993.

Ponte, R. M., Understanding the relation between wind- and pressure-driven sea level variability, *J. Geophys. Res.*, *99*, 8033–8039, 1994.

Ponte, R. M. and R. D. Rosen, Oceanic angular momentum and torques in a general circulation model, *J. Phys. Oceanogr.*, *24*, 1966–1977, 1994.

Ponte, R. M., D. Stammer, and J. Marshall, Oceanic signals in observed motions of the Earth's pole of rotation, *Nature*, 476–479, 1998.

Semtner, A. J., and R. M. Chervin, Ocean general circulation from a global eddy-resolving model, *J. Geophys. Res.*, *97*, 5493–5550, 1992.

Stammer, D., R. Tokmakian, A. Semtner, and C. Wunsch, How well does a 1/4° global circulation model simulate large-scale oceanic observations? *J. Geophys. Res.*, *101*, 25779–25812, 1996.

vanDam, T. M., and T. A. Herring, Detection of atmospheric pressure loading using very long baseline interferometry measurements, *J. Geophys. Res.*, *99*, 4505–4517, 1994.

van den Dool, H. M., and S. Saha, Seasonal redistribution and conservation of atmospheric mass in a general circulation model. *J. Climate*, *6*, 22–30, 1993.

White, W. B., and C. K. Tai, Inferring interannual changes in global upper ocean heat storage from TOPEX altimetry, *J. Geophys. Res.*, *100*, 24943–24954, 1995.

Wang, L., and C. Koblinsky, Can the Topex/Poseidon altimetry data be used to estimate air-sea heat flux in the North Atlantic? *Geophys. Res. Lett.*, *24*, 139–142, 1997.

Willebrand, J., S. G. H. Philander, and R. C. Pacanowski, The oceanic response to large-scale atmospheric disturbances, *J. Phys. Oceanogr.*, *10*, 411–429, 1980.

Woodworth, P.L., J.M. Vassie, C.W. Hughes, and M.P. Meredith, A test of the ability of TOPEX/POSEIDON to monitor flows through the Drake Passage, *J. Geophys. Res.*, *101*, 11935–11947, 1996.

Wunsch, C., and D. Stammer, Atmospheric loading and the oceanic "inverted barometer" effect, *Rev. Geophys.*, *35*, 79–107, 1997.

R. M. Ponte, Atmospheric and Environmental Research, Inc., 840 Memorial Drive, Cambridge, MA 02139 USA. (e-mail: ponte@aer.com)

–; revised –; accepted –.

This preprint was prepared with AGU's LaTeX macros v4. File temp formatted November 2, 1998.

Figure 1. Time series of $\overline{\zeta_\rho}$ (cm) for the period January 1989–December 1994 calculated from POCM output as described in the text. Origin of the time series is arbitrarily set to zero.

Figure 2. Anomalies in p_b averaged over the months of December-February, March-May, June-August, and September-November. Contour interval is 0.5 cm; negative values are lightly shaded.

Figure 3. Power spectrum obtained by averaging individual periodograms of p_b (no area weighting) calculated at all model points. No averaging in frequency is applied.

Figure 4. Anomalies in p_b as in Fig. 2, but calculated from the barotropic model based on two years of output (1993–1994). Countour intervals are 1 cm; negative values are lightly shaded. Dark shading represents land points in the model.

Figure 5. Anomalies in p_b as in Fig. 2, but calculated from the POCM model based on only two years (1993–1994). Countour intervals are 1 cm; negative values are lightly shaded.

Figure 6. Seasonal anomalies in the Ekman pumping forcing term in (1), based on wind values for 1993–94. Values within 5° of the equator were not calculated. Countour interval is 10^{-4} g s^{-2}; negative values are lightly shaded. The land mask is that of the barotropic model in Fig. 4.

Figure 7. Power spectrum of the Ekman pumping term in (1), calculated by averaging periodograms at all points for which data is shown in Fig. 6. No averaging in frequency is applied.

Plate 1. Amplitude (in cm) and phase of the annual cycle in p_b. Note the changing contour intervals for the amplitude. Phases are plotted every other point and indicated by the direction of the line segments (origin denoted by the dots); 0° corresponds to eastward direction, and phase increases anticlockwise. Values between $-45°$ and 45° correspond approximately to a maximum in northern winter season (Dec–Feb), between 45° and 135° to a maximum in northern spring, and so on.

Plate 2. Amplitude and phase of the admittance between p_b and ζ' for the annual harmonic. Phase is plotted as in Plate 1. Line segments pointing eastward (westward) imply in-phase (out-of-phase) relation between p_b and ζ'.

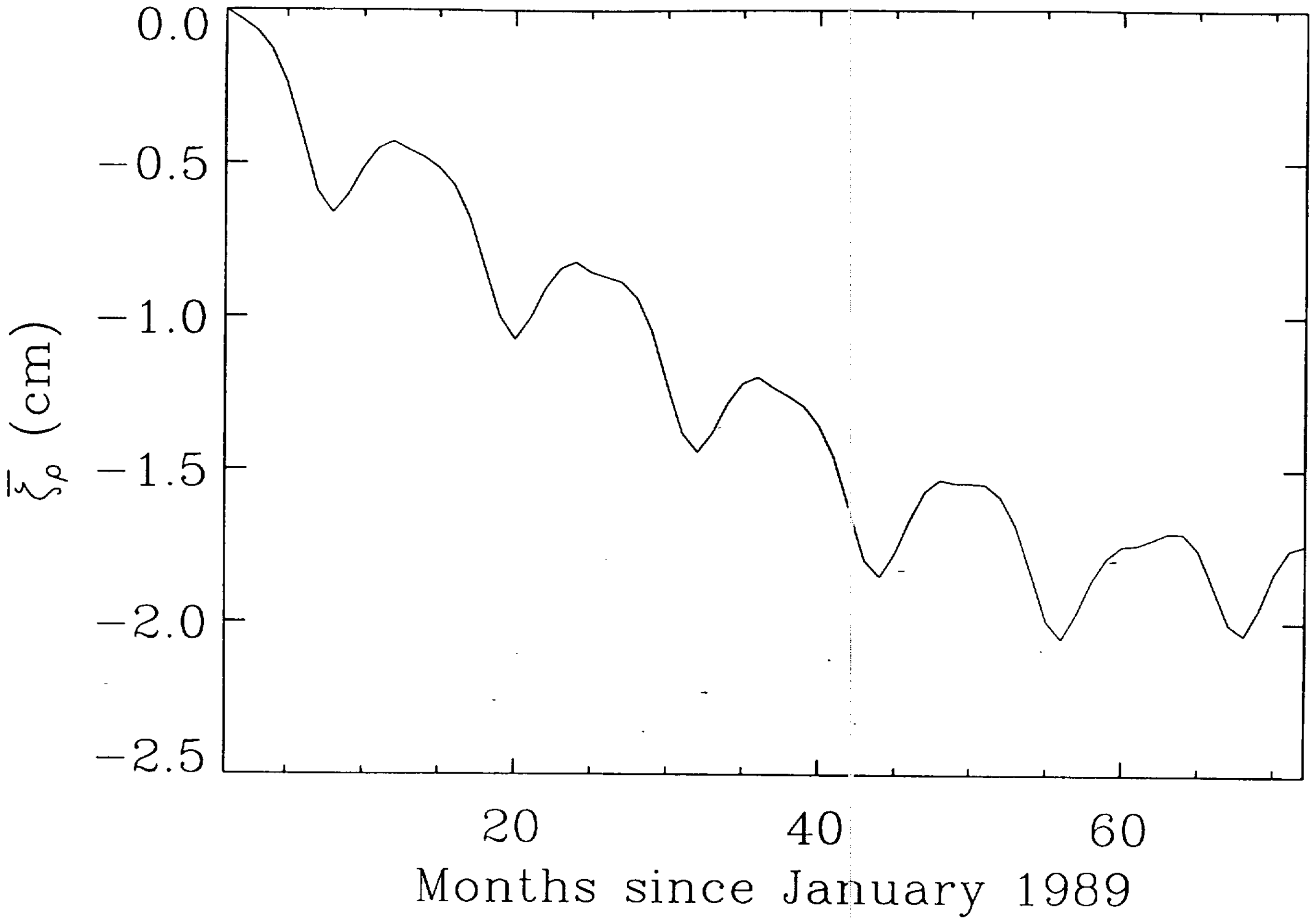
0.0
−0.5
−1.0
−1.5
−2.0
−2.5
$\bar{\xi}_\rho$ (cm)
20
40
60
Months since January 1989

Fig. 1

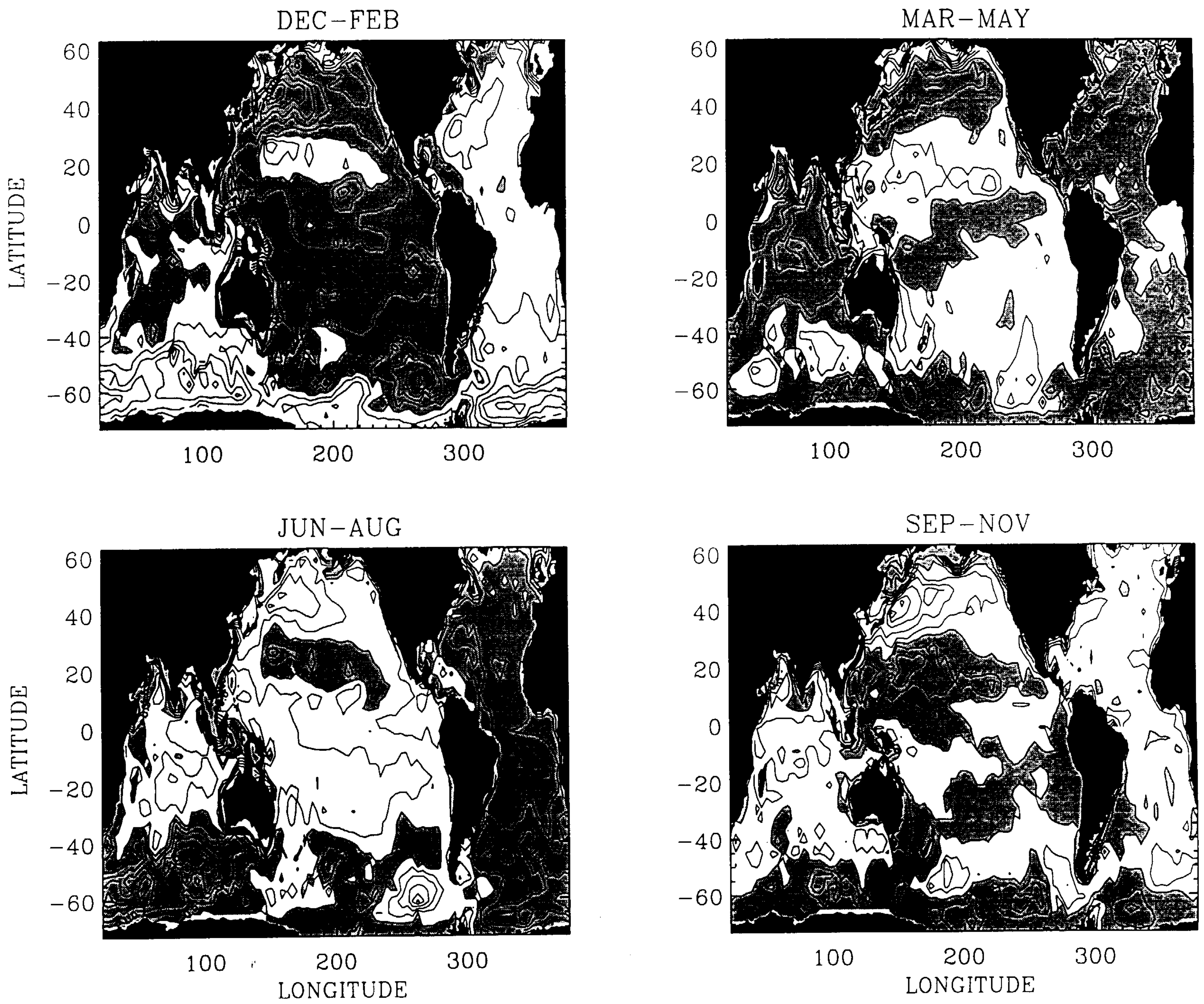
DEC−FEB
MAR−MAY
JUN−AUG
SEP−NOV
LATITUDE
LATITUDE
60
40
20
0
−20
−40
−60
100
200
300
LONGITUDE
LONGITUDE

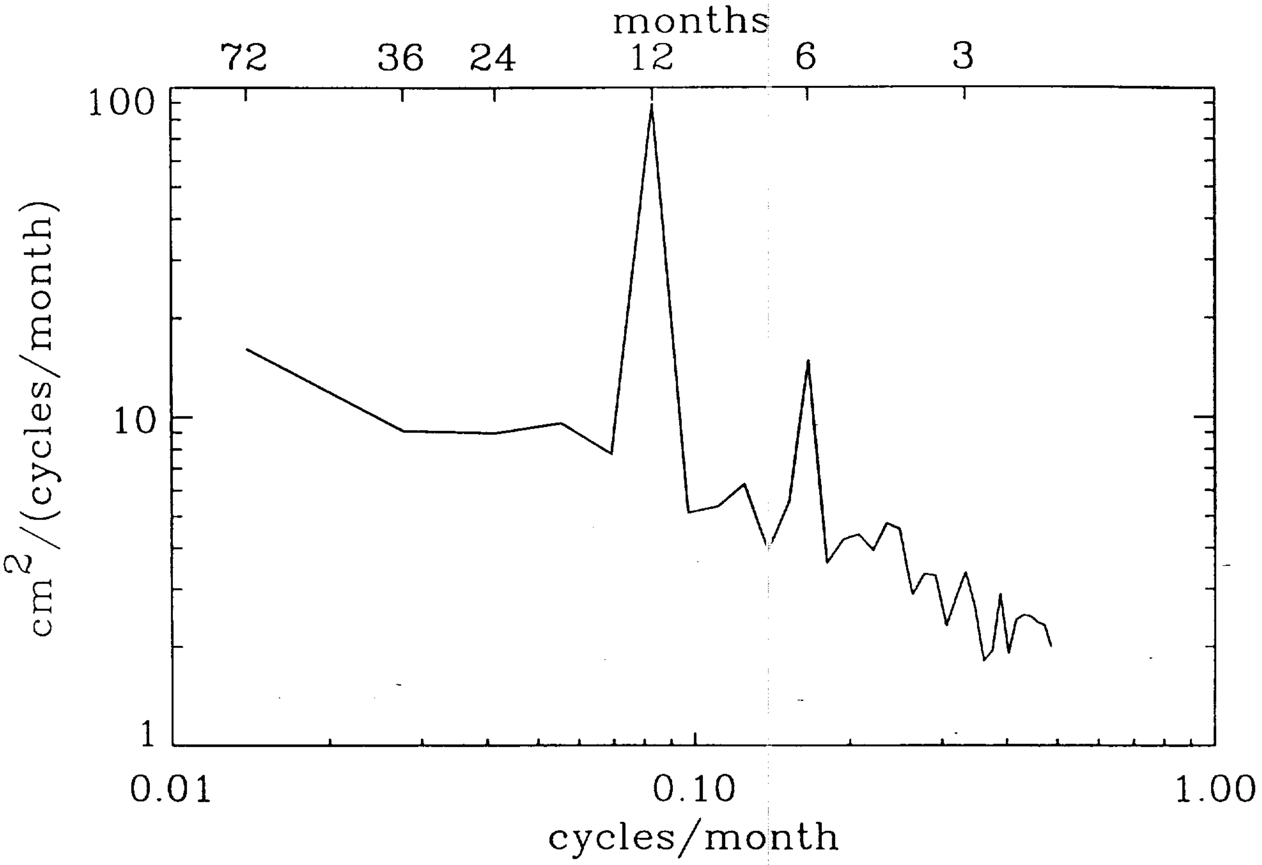
months
72
36
24
12
6
3
100
10
1
cm^2/(cycles/month)
0.01
0.10
1.00
cycles/month

Fig. 5

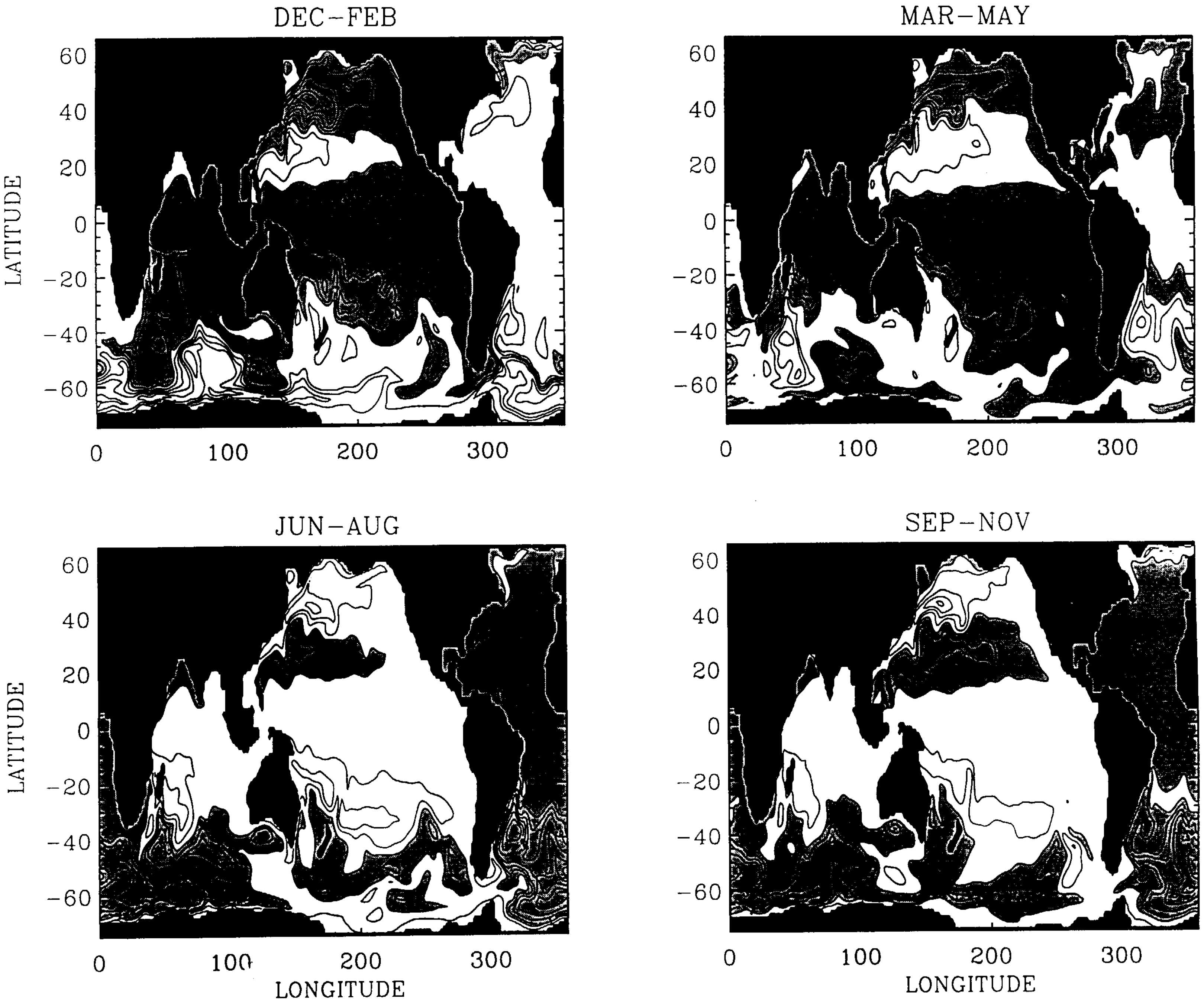
DEC-FEB
MAR-MAY
JUN-AUG
SEP-NOV
LATITUDE
LATITUDE
60
40
20
0
-20
-40
-60
0
100
200
300
LONGITUDE
LONGITUDE

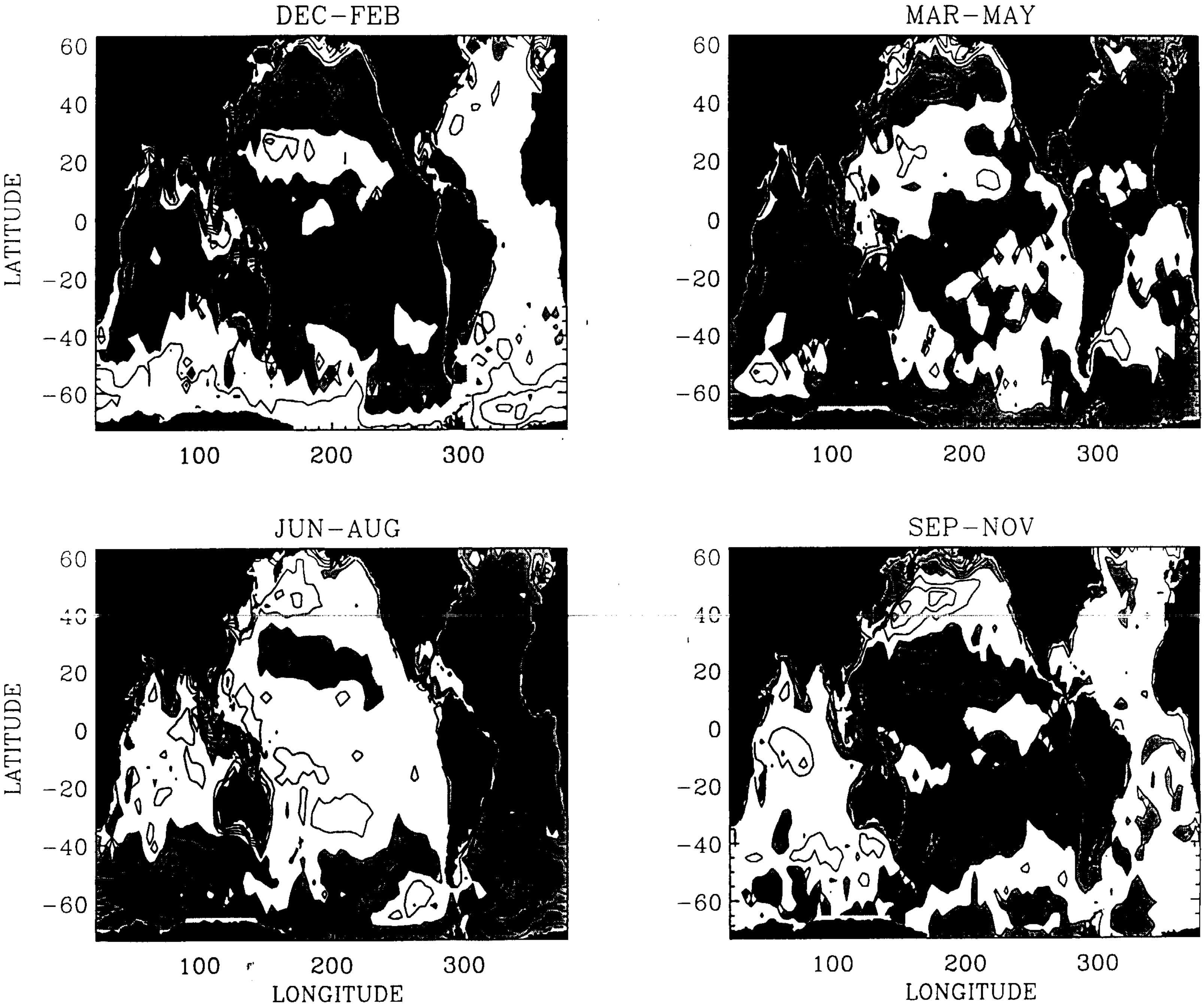
DEC-FEB
MAR-MAY
JUN-AUG
SEP-NOV
LATITUDE
60
40
20
0
-20
-40
-60
100
200
300
LONGITUDE

Fig. 7

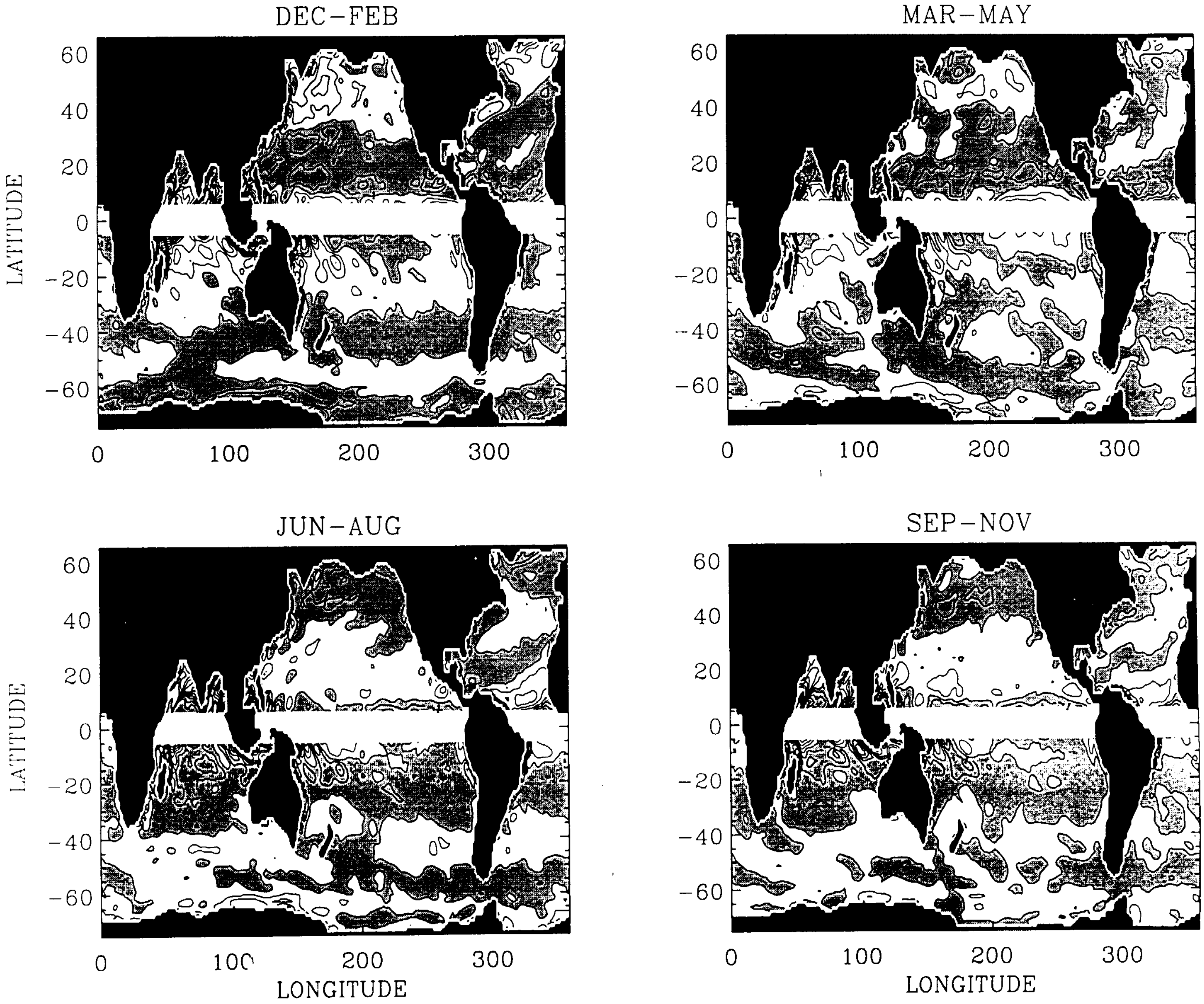
DEC-FEB
MAR-MAY
JUN-AUG
SEP-NOV
LATITUDE
LATITUDE
60
40
20
0
-20
-40
-60
0
100
200
300
LONGITUDE
LONGITUDE

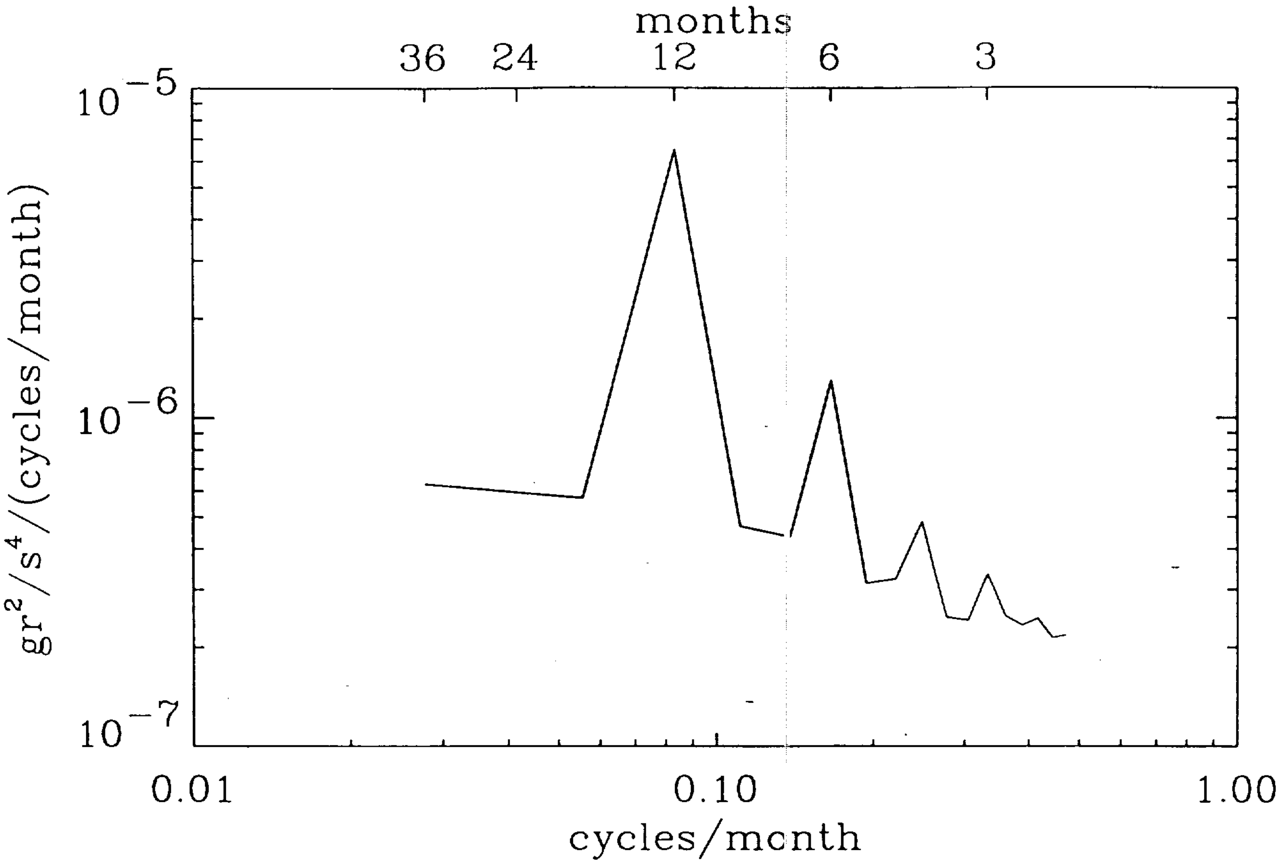
months
36
24
12
6
3
10^{-5}
10^{-6}
10^{-7}
gr^2/s^4/(cycles/month)
0.01
0.10
1.00
cycles/month

Fig. 7

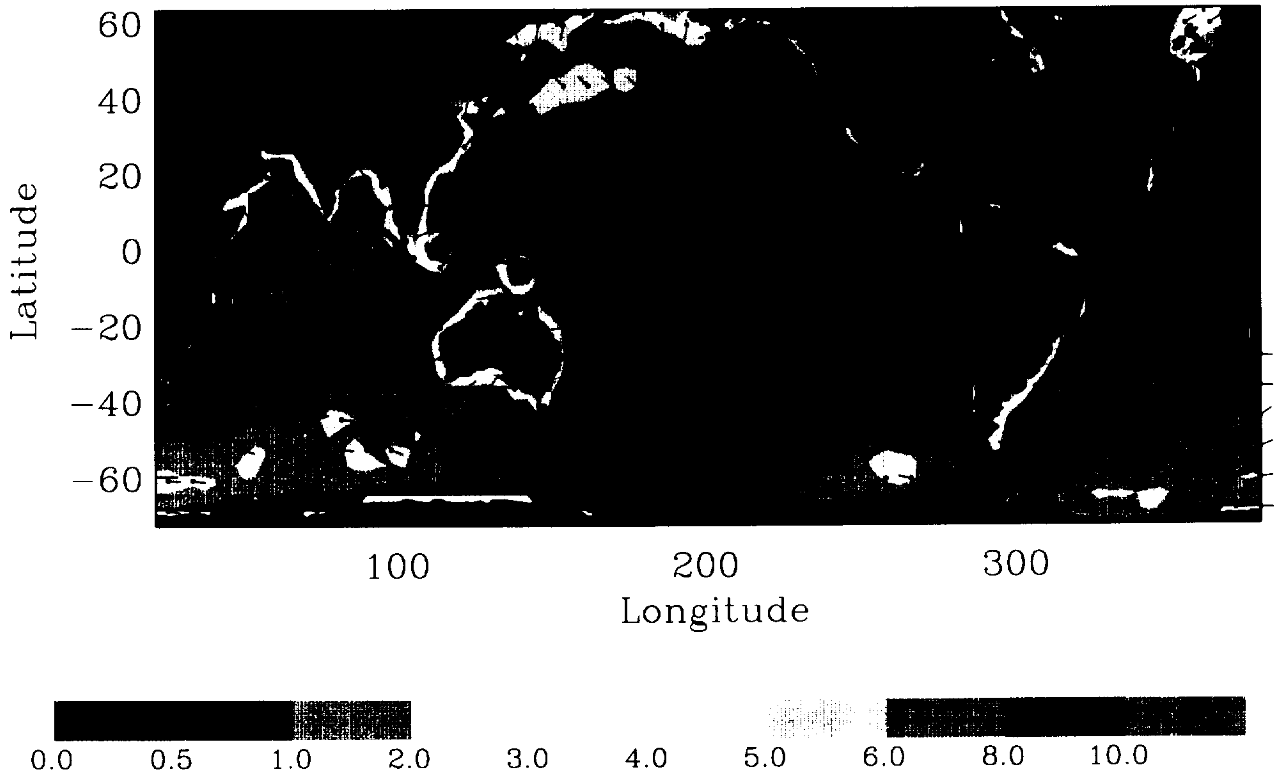
60
40
20
0
−20
−40
−60
Latitude
100
200
300
Longitude
0.0
0.5
1.0
2.0
3.0
4.0
5.0
6.0
8.0
10.0

Plate 1

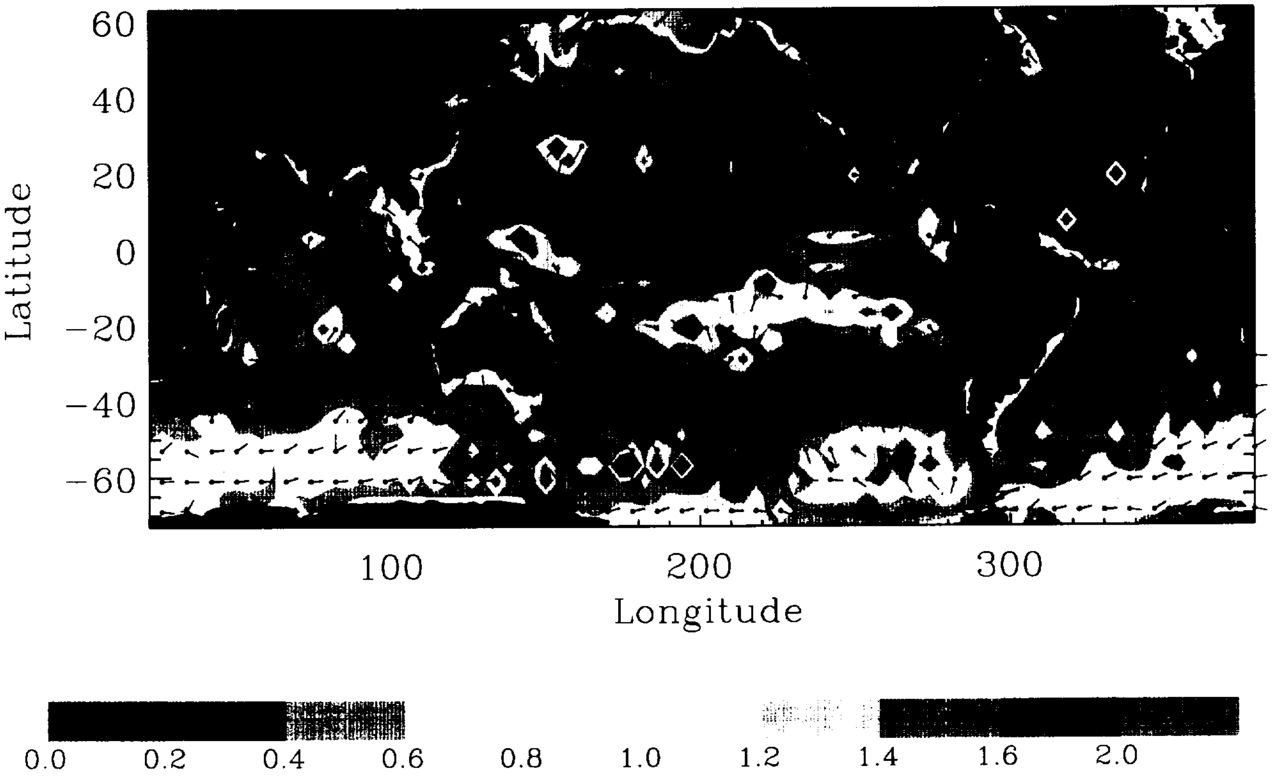
60
40
20
0
−20
−40
−60
Latitude
100
200
300
Longitude
0.0
0.2
0.4
0.6
0.8
1.0
1.2
1.4
1.6
2.0

Plate 2